Chapter 8

Review: Physicochemical Structure Effects on Metal Oxide Nanoparticulate Cytotoxicity

Charles C. Chusuei,*,[1] Chi-Heng Wu,[2] Shravan Mallavarapu,[1] Fang Yao Stephen Hou,[3] Chen-Ming Hsu,[4] Robert S. Aronstam,[2] and Yue-wern Huang[2]

**[1]Department of Chemistry, Middle Tennessee State University,
440 Friendship Street, Murfreesboro, Tennessee 37132, U.S.A.
[2]Department of Biological Sciences,
Missouri University of Science and Technology,
400 W. 11th Street, Rolla, Missouri 65409, U.S.A.
[3]Department of Clinical Laboratory Science, Marquette University,
P.O. Box 1881, Milwaukee, Wisconsin 53201, U.S.A.
[4]Department of Life Science, National Taiwan Normal University,
88 Ting-Chow Rd, Sec 4, Taipei 116, Taiwan, ROC
*E-mail: Charles.Chusuei@mtsu.edu.**

The utility of physicochemical surface characterization as a tool for understanding surface structure-property relationships governing fourth period metal transition metal oxide nanoparticulate (TiO_2, Cr_2O_3, Mn_2O_3, Fe_2O_3, NiO, CuO and ZnO) cytotoxicity is shown. An overview of surface structural probes of the material isoelectric point and relative number of binding sites on the oxide surface is presented, relating these factors with observed trends in toxicity. A tutorial is given explaining the strategy used to probe the solid surface, and correlating nanoparticulate physicochemical structure with cytotoxicity. Insight into the role of nanoparticle (NP) surface charge and relative number of binding sites are applied for interpreting two case studies showing (1) enhanced toxicity of TiO_2 NPs (the least toxic NPs in the series), and (2) mitigating potent toxicity of ZnO NPs.

Introduction

Currently, there are more than 2800 nanoparticulate-based commercial applications. By 2017, its world-wide market is estimated to be $48.9 billion (*1*). As the use of nanoparticulates proliferate, an understanding of their environmental and health impact, and their effects on biological systems become increasingly important. Nanoparticles (NPs) are used in a wide variety of applications, including catalysis (*2–4*), magnetocooling (*5*), optical recording devices (*6*, *7*), purification of enzymes and other biological materials (*8*), water purification devices (*9*), magnetic field assisted radionuclide therapy (*10*), cosmetic and skin care products (*11*), and targeted drug delivery agents (*12*, *13*). Yet, there is a paucity in understanding the physicochemical surface structure governing the cytotoxicity of these materials. Variation in degrees of metal oxide particulate toxicities have been documented. Toxicological studies with cell cultures and animal models indicate that nanoparticles (NPs) are more inflammogenic and toxic than their bulk counterparts of equal mass (*14*). Intricate relationships between NPs, changes in intracellular Ca^{2+}, and production of reactive oxygen species (ROS) have been shown by Huang et al. (*15*); these studies show that NPs can trigger cell death by various pathways. NPs are known to increase intracellular Ca^{2+} concentration. Moderation of this increase by nifedipine suggests an influx of extracellular calcium. Membrane disruption, as shown by membrane depolarization and lipid peroxidation, may play an active role in this influx. In addition, NPs can disrupt store-operated calcium entry (*16*).

To delineate physicochemical factors governing toxicity, we explore the effects of nanoparticulate surface charge and relative number of binding sites on the metal oxide nanoparticulate surface on cellular toxicity. We focus our study on an array of fourth period transition metal (within the periodic table) oxides, i.e., those oxides of Ti, Cr, Mn, Fe, Ni, Cu and Zn, all of which currently have wide commercial applications.

Noteworthy is that during these investigations, we have employed an underutilized, but powerful tool of ultra-high vacuum (UHV)-based surface characterization to explore interactions at the solid-liquid interface after exposure to physiological (aqueous solution) conditions. A critique of using this approach is that UHV conditions (i.e., 10^{-8} to 10^{-10} Torr pressure) are far removed from realistic conditions of biological systems, especially since equilibrium between the solid surface and aqueous solution interface is interrupted. Despite these concerns, past studies have shown that *ex situ* charged particle surface probes, such as Auger electron (AES) and X-ray photoelectron spectroscopies (XPS), can still be used to quantify adsorption of oxygen-containing species taking place in aqueous solution on metal oxide surfaces by examining the integrated photoelectron peak areas (*17–19*). The role of stabilized pH, which exists for buffered physiological environments, have been only sparsely explored, i.e., pH = 7.4 to simulate cystolic environments, and pH = 4.5 for lysosomal ones.

Experimental Procedures

Chemicals and Materials

Transition metal oxide NPs (TiO_2, Fe_2O_3, NiO, Mn_2O_3, CuO, and ZnO) were purchased from Nanostructured and Amorphous Materials (99.9% purity; Los Alamos, New Mexico, U.S.A.) and used as received. Ham's F-12 medium with L-glutamine was purchased from Fisher Scientific (Pittsburgh, PA, U.S.A.). Fetal bovine serum, human bronchoalveolar carcimoma-derived (A549) cells, and immortalized human bronchial epithelial cells (BEAS-2B) were purchased from the American Type Culture Collection (ATCC) (Manassas, VA, U.S.A.). Trypsin-EDTA and Hank's balanced salt solution (HBSS were purchased from Invitrogen (Carlsbad, CA, U.S.A.). Ultrapure DI-water was prepared using a Milli-Q system (Millipore, Bedford, MA, U.S.A.). Sulforhodamine B (SRB) was purchased from ICN Biomedicals (Irvine, CA, U.S.A.).

X-ray Photoelectron Spectroscopy (XPS)

Surface analysis of the metal oxide NPs was performed using XPS. Reacting the metal oxide NPs under long-term pH controlled conditions, using a constant composition (CC) apparatus, was conducted as follows. Transition metal oxide NPs were reacted in a 702 Titrino MetroOhm AG CH-9191 CC reactor (Herisau, Switzerland) adjusted to pH = 7.4 (± 0.1), and maintained for a 24-hr period. Using the autotitrator, HCl or NaOH was added dropwise to maintain constant pH. All solutions were prepared using doubly distilled, deionized Millipore water as the solvent. The CC reactor colloidal suspensions were prepared by adding 125 mg of the metal oxide to 25.0 mL of 0.01 M NaCl solution (with NaCl serving as background electrolyte) (*18*, *19*) to stabilize pH. Solutions were stirred during the CC reactions. Solid samples of metal oxide NPs (from each 16-hr batch solution reaction) were then extracted via vacuum filtration and saved for subsequent XPS analysis.

Microscopy and Brunauer−Emmett−Teller (BET) Surface Area Measurements

Particle morphology and size were characterized using transmission electron microscopy (TEM) with a JEOL 1400 instrument (JEOL U.S.A., Inc.; Peabody, MA, U.S.A.) operated at 120 kV. To prepare samples for imaging, 1 mg of each transition metal oxide NP sample was placed in 1 mL of doubly distilled deionized water, respectively, in an Eppendorf tube and sonicated; 1-μL aliquots were then applied to 400-mesh carbon coated copper grids (Electron Microscopy Sciences, Hatfield, PA, U.S.A.) and allowed to dry in N_2 environment prior to microscopy. TEM images were analyzed using ImageJ ver. 1.44 software (National Institutes of Health, Gaithersburg, MD, U.S.A.) for morphology analysis and individual particle size measurements. Brunauer−Emmett−Teller (BET) specific surface area (SSA, m^2/g) measurements were obtained using a Quantachrome Autosorb 1-C instrument (Quantachrome Corp.; Boynton Beach, FL, U.S.A.) and N_2 as the probe molecule (*20*).

The point-of-zero charge (PZC) is the pH value at which the solid surface is electrostatically neutral under aqueous solution conditions due to absorption of equal amounts of hydronium and hydroxyl ions at the electrical double layer (*21*). The pH at the solid surface-aqueous solution interface was measured using a spear tip electrode, based on the original description by Park and Regalbuto (*22*), and modified for use to measure PZC of nanomaterials in our laboratory (*23*). The procedure is as follows. Solutions in the range of pH = 1.0–13.0 were prepared by adding dilute aqueous solutions of NaOH and HCl until the desired initial pH is obtained. For each reading, a 1.8-mL aliquot of each solution was pipetted into 2-mL polyethylene vials and allowed to equilibrate for 1 hr. The initial pH of each solution was measured and recorded. A 10.0-mg amount of each metal oxide NP powder was then added to each solution, and allowed to settle to the bottom of the polyethylene tube. After an additional 16-hr equilibration period, the final pH of the nanoparticle surface was again measured using a spear tip semisolid electrode. Plots of initial versus final pH values reveal plateaus denoting the isoelectric point, denoted by the PZC, for each metal oxide.

The relative number of available particle surface binding sites on the NP surfaces were quantified using integrated XPS peak areas of the O 1s orbital of the nanoparticle surfaces, acquired using a Kratos Axis 25 XPS spectrometer (Kratos Analytical; Manchester, U.K.). In our experiments, the different oxidation states of the O 1s orbital peaks were deconvoluted to determine the contributions of metal oxide oxygen of the NP solid surface and non-metal oxide species adsorbed to the overall peak envelope. In all spectral studies, the limiting case that all non-metal oxide oxidation states denote adsorption to available sites on the NP surface is assumed.

Surface Analysis of the NP Solid Surface

NPs were collected from the CC reservoir by vacuum filtration using a Buchner funnel and a Fluoropore PTFE membrane filter paper with a 0.2 µm pore size (Billerica, MA, U.S.A.). The NP solids were then mounted onto the XPS sample holder for spectral analysis by cutting the membrane filter (onto which the metal oxide NPs were collected via vacuum filtration) into 1 cm × 1 cm x 0.1 mm squares and affixing the Teflon filter paper onto the holder with double-sided tape. Charge correction was performed using the C 1s binding energy at 284.7 eV, denoting adventitious carbon from the atmosphere (*24*, *25*). XPS scans were obtained using a Mg Kα anode operated at 225 W and a photon energy of hν = 1253.6 eV. Peaks were then deconvoluted using CasaXPS VAMAS processing software (Devon, U.K.) and 70:30 Gaussian-Lorenztian lineshapes and using Shirley background subtractions (*26*). Integrated peak area ratios of the physisorbed-to-metal oxide oxygen, obtained from curvefitting deconvoluted oxidation states from the XPS O 1s core level. The integrated peak area ratio of the metal oxide oxidation state versus that of the absorbed oxygen from the O 1s orbital was used to quantify the relative number of binding sites (*18*, *19*).

Cytotoxicity Assay and Apoptosis Measurements

Cells were fixed with cold 10% trichloroacetic acid (TCA) for 1 hr at 4ºC. The TCA solution was then discarded, and the cells were washed three times with distilled water, followed by complete drying. Sulforhodamine B (0.2% in 1% acetic acid) was then added to stain the cells for 30 min at room temperature. At the end of exposure to NP suspensions, the medium was discarded. Sulforhodamine B assay was used to determine cell viability relative to the control group (27). The staining solution was then discarded and the cells were washed with 1% acetic acid three times to eliminate excess dye. After complete drying, the dye was dissolved in cold 10 mM Tris buffer (pH =10.5). Aliquots (100 µL) of dye solution were then transferred onto a 96-well plate, and absorbance was measured at 550 nm using a microplate reader (FLOURstar, BMG Labtechnologies; Durham, NC, U.S.A.). Morphological examination of apoptotic cells were performed using annexin V-FITC and 7-aminoactinomycin D (7-AAD) dyes for staining and observing them with an Olympus IX 51 epifluorescence microscope. The stain dyes were also used to quantify the cells using a Beckman Coulter Cell Lab Quanta SC system.

Statistical Analysis

Spearman's Rank Correlation Analysis (ρ) is used to correlate cytotoxicity with surface charge and relative number of surface binding sites. For cytotoxicity studies, three independent experiments were conducted in triplicate for each treatment group, with data expressed as the mean ± standard deviation (SD).

Results

The morphologies of NPs observed with TEM are needle-like (TiO_2), spherical (Mn_2O_3, Fe_2O_3), or nearly spherical (Cr_2O_3, NiO, CuO, ZnO). Approximate physical sizes (APS) of the seven commercially available transition metal oxide NPs ranges from 16 ± 5 nm (NiO) to 82 ± 31 nm (Mn_2O_3) (Table 1). Specific surface areas (SSA) of the NPs ranges from 8.71 m^2/g (Mn_2O_3) to 178.95 m^2/g (TiO_2). While TiO_2, Fe_2O_3, and CuO have similar sizes, all of the NPs possessed distinctly different specific surface areas, owing to variations in surface porosity and morphology.

Metal oxide NPs reacted with two human lung cell lines, A549 and BEAS-2B, were tested to ascertain whether cytotoxicity is cell-type specific among non-phagocytic cells (28). A 24-hr study of A549 cells exposed to NPs reveals a trend of toxicity (Figure 1). An identical trend of cytotoxicity is observed for both A549 and BEAS-2B cell lines. Identical trends between these two fundamentally different cell lines indicate that NP cytotoxicity is not cell-type specific for these non-phagocytic cell lines. The highest concentration tested is 100 µg/mL, above which cells become engulfed by NPs. The TiO_2 NPs shows little, if any, signs of toxicity at a 100 µg/mL concentration compared to the control group while CuO showed potent toxicity at a significantly diminished concentration (20 µg/mL). Note that the increase in cell viability in the media with TiO_2 is a result of cell growth, which continues in the presence of these NPs.

Table 1. Measured Specific Surface Areas, Approximate Physical Size, and Morphology of Nanoparticles. Reproduced with permission from reference (*28*). Copyright 2013 Elsevier.

	TiO_2	Cr_2O_3	Mn_2O_3	Fe_2O_3	NiO	CuO	ZnO
APS (nm)	46±20	63±34	82±31	48±13	16±5	47±24	27±13
SSA (m^2/g)	178.95	11.41	8.71	31.44	70.86	9.02	44.61
shape	needle-like	nearly spheri-cal	spheri-cal	spheri-cal	nearly spheri-cal	nearly spheri-cal	nearly spheri-cal
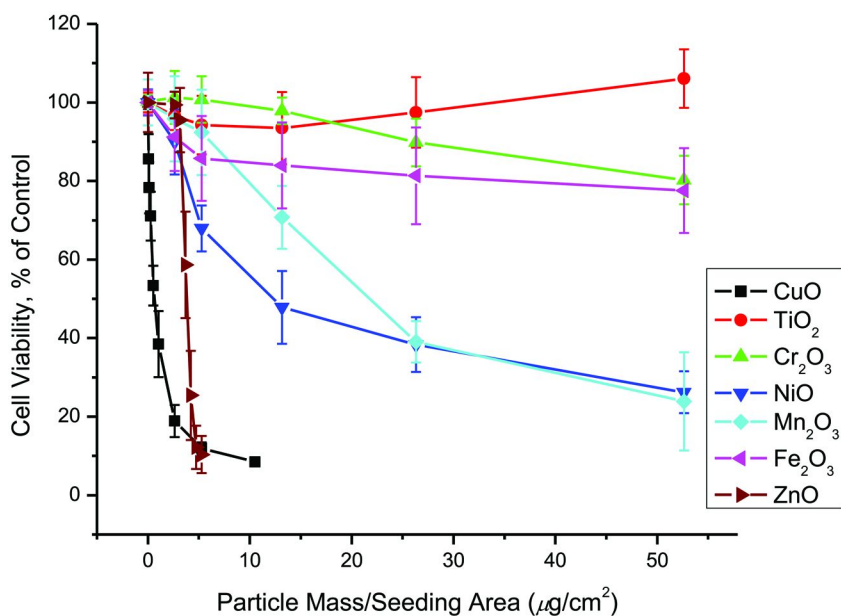
Figure 1. Morphology and size distribution of 4th period metal oxide NPs. Reproduced with permission from reference (28). Copyright 2013 Elsevier. (see color insert)

Observed toxicity falls into three categories: (i) TiO_2, Cr_2O_3, and Fe_2O_3 have zero-to-minimal toxicity (close to 100% cell viability); (ii) Mn_2O_3 and NiO show typical dose-dependent toxicity (~ 40% cell viability); and (iii) CuO and ZnO induce potent toxicity within a narrow dose range (≤ 20% cell viability). Cytotoxicity is observed in the form of apoptosis (Figure 2). Both CuO and ZnO results in toxicity with a steep concentration range. Despite differences in SSA and morphology of the metal oxide NPs in this series (Table 1), no correlation is observed between measured SSA or morphology with relative degree of cytotoxicity based on these parameters (Figure 2) (*28*).
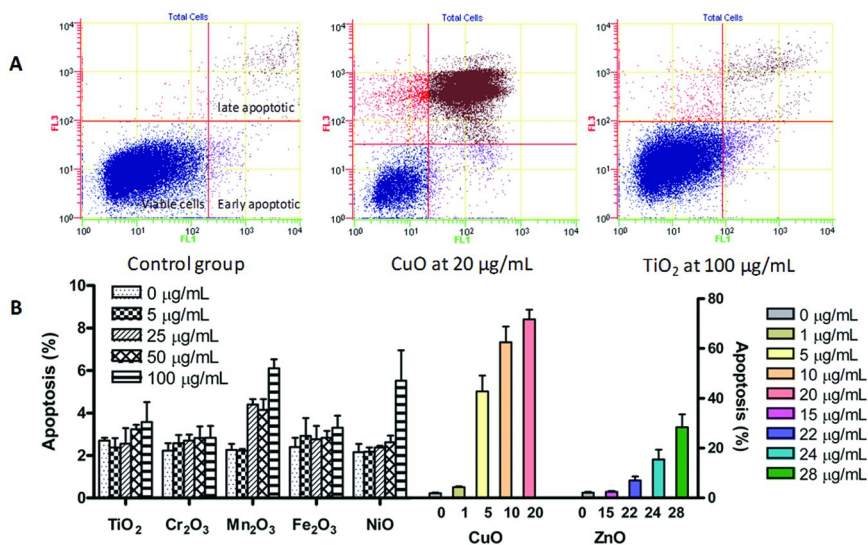
Figure 2. Transition metal NPs induces cell death in A549 cells: (A) AV positive/7-AAD negative (apoptotic) and AV-positive/7AAD positive (late apoptosis, early necrosis); (B) Percentage of late apoptotic and early necrotic populations. Adapted with permission from reference (28). Copyright 2013 Elsevier. (see color insert)

Correlating Physicochemical Properties with NP Toxicity

Two parameters, in particular, are examined with regard to its respective effects on cytotoxicity: (i) surface charge at the solid-aqueous solution interface, and (ii) relative number of available surface binding sites. Particle surface charge, measured as PZCs, of the metal oxides are summarized in Figure 3. Horizontal dashed lines within the PZC plot at pH = 4.5 and 7.4 denote the pH of the lysosomal and cytosolic environments, respectively. Noteworthy is the fact that as PZC increases, the cytotoxic effects of the NPs on the BEAS-2B and A549 cell lines increase, except for Mn_2O_3. Most of the PZC values are clustered between PZC values of 8 and 9, above both lysosomal and cytosolic environments, with the exception of TiO_2, which has a PZC of 6.9. There is good correlation between cytotoxicity and PZC, with Spearman's Correlation Rank values of $\rho = 0.94$ (calculated with Mn_2O_3 as an outlier) and $\rho = 0.78$ (without Mn_2O_3 as an outlier). Cytotoxicity of the metal oxide NPs in both cell lines correlates with their respective PZCs. Noteworthy is the fact that TiO_2 has a PZC of 6.9 while the pH of cell medium (with the presence of cells) is 7.4, similar to that of the cytosol. The lowered PZC of the TiO_2 NPs indicates that they would be populated with a negatively charged species due to Coulombic attractions, leading to low cellular uptake that requires crossing a negatively-charged cytoplasmic membrane. The

explanation of lower bioavailability is limited by the fact that NPs could be coated by proteins in cell culture medium to form protein corona, which would influence surface charge.
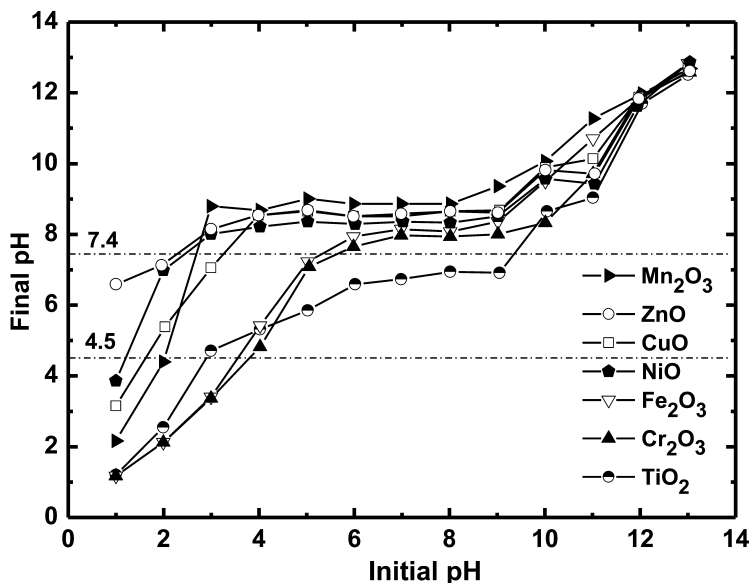

Figure 3. PZC initial pH versus final pH plots of Mn_2O_3, ZnO, CuO, NiO, Fe_2O_3, Cr_2O_3, and TiO_2 metal oxide NPs. Horizontal lines at pH 7.4 and pH 4.5 denote cystolic and lysosomal environments, respectively. Reproduced with permission from reference (28). Copyright 2013 Elsevier.
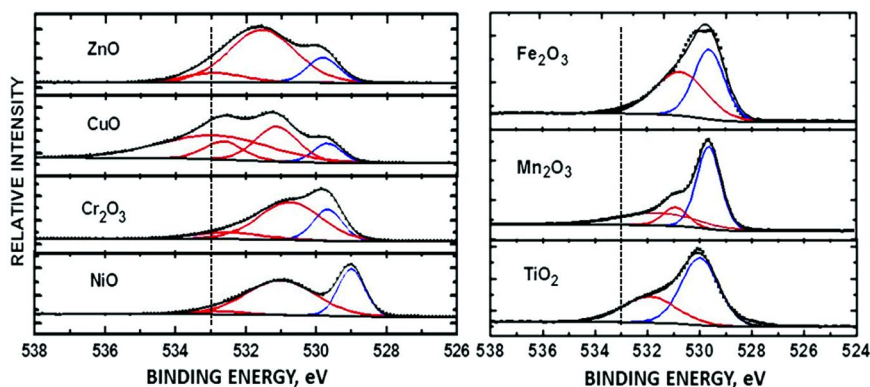

Figure 4. XPS of O 1s orbitals of ZnO, CuO, Cr_2O_3, NiO, Fe_2O_3, Mn_2O_3, and TiO_2 NPs. Reproduced with permission from reference (28). Copyright 2013 Elsevier. (see color insert)

Relative Number of Surface Binding Sites

The relative number of available particle surface binding sites are quantified by XPS. A greater physisorbed-to-metal oxide oxygen ratio denotes more adsorption sites potentially available for cellular molecular binding. Figure 4 shows a stack plot of XPS spectra of the O 1s orbitals of all NPs following a 16-hr CC reaction at pH = 7.4. The chemical oxidation state denoting metal oxide is clearly defined for each metal oxide NP. The XPS binding energies (BEs) with full-width-at-half-maxima (fwhm) in parentheses are found to be at 530.0 (1.7), 529.6 (1.1) and 529.5 (1.4) eV, in agreement with literature values for the metal oxide oxidation state for TiO_2 (*19*), Mn_2O_3 (*29, 30*), and Fe_2O_3 (*31, 32*), respectively. BEs observed at 531.9 (2.4) eV for adsorbates on TiO_2 (*33–35*), 530.9 (1.1) and 531.5(4.0) eV on Mn_2O_3, and 529.5 (1.4) and 530.6 (2.4) eV on Fe_2O_3 are consistent with adsorbed hydroxyl species on these surfaces (*36*). BEs of the metal oxide chemical state observed at O 1s = 529.0 (0.9), 529.7 (1.0), 529.7 (1.0), and 529.8 (1.1) eV match literature values for NiO (*37*), Cr_2O_3 (*38*), CuO (*39, 40*), and ZnO (*41*), respectively. BE peak centers at 531.0 (2.3) eV for adsorbates on NiO, 530.7 (2.1) and 532.5 (2.3) eV on Cr_2O_3, 531.1 (1.4) eV on CuO and 531.6 (2.2) eV on ZnO are also consistent with the presence of surface adsorbed hydroxyls. The vertical dashed line (Figure 4) denotes the BE chemical shift for the H_2O oxidation state. The O 1s BE peak centers at 532.9 (1.7) eV for adsorbates on NiO, 532.5 (2.3) eV on Cr_2O_3, 532.6 (1.3) and 532.9 (3.7) eV on CuO, and 532.9 (2.0) eV on ZnO denote adsorbed H_2O on these surfaces (*33, 36*). There is good correlation between cytotoxicity and available nanoparticle surface binding sites ($\rho = 0.71$). According to these data, the relative number of available binding sites (Table 2) for each oxide is in the following ascending order: $TiO_2 <$ $Mn_2O_3 < Fe_2O_3 < NiO < Cr_2O_3 < CuO < ZnO$. A correlation between the increase in relative number of binding sites with PZC (Figure 3) is also observed. As PZC increases there is a corresponding increase in Coulombic attraction with negatively charged extracellular material at pH = 7.4. The increase in surface binding of oxygen-containing material (and hence the larger number of occupied surface binding sites) is attributed to be a result of greater Coulombic attraction of material to the NP surface.

As NP size decreases, the NP surface area-to-bulk ratio increases significantly, providing potential sites for interaction with biomolecules such as lipids, DNA, RNA and protein. XPS is used to estimate the relative number of available surface binding sites, we attribute the changes in the O 1s line shapes (not emanating from the metal oxide oxidation state) to weakly adsorbed O-containing moieties at the metal oxide NP surface. The adsorbates are predominantly H_2O and hydroxyl groups; however, CO and CO_2 from atmosphere can also adsorb to the surface. Their binding energies (BEs) typically overlap with observed chemical shifts for adsorbed hydroxyls in the ~531 eV region (*36*). Variations in the number of available surface sites can be attributed to the atomic level structures of the lattice oxygens within each oxide (*42*). A periodic trend of increasing adsorbed-to-metal oxide oxygen is observed for the series of metal oxides studied, with the exception of Cr_2O_3, which deviates in that it has a pronounced amount of adsorbed oxygen, likely due to an artifact of CO_2 from solution exposure to the atmosphere. CO_2 has

a propensity to adsorb onto Cr_2O_3. The relatively large XPS intensity at O 1s BE at 531.2 eV (Figure 4) has also been reported to emanate from a mixed complex of $Cr_2O_3 \cdot nH_2O \cdot xCO_2$ formed from adsorbed atmospheric CO_2 into the aqueous solution (*43*). The most toxic of nanoparticles analyzed in this series also has the highest adsorbed H_2O content. The vertical, dashed line (Figure 4) denotes the chemical oxidation state for adsorbed H_2O. ZnO and CuO have the highest PZCs and hence greatest degree of "protonation" via adsorption of hydronium ions (H_3O^+). Under aqueous solution physiological conditions, the metal oxide surface would be populated by excess H_3O^+, in accordance with Gouy-Chapman theory. During adsorption, the adsorbate would be electrically neutralized resulting in the observed, enhanced intensity denoting chemisorbed H_2O at 532.9 eV on the CuO and ZnO surfaces. Adsorbed H_2O is not pronounced on the Cr_2O_3, Mn_2O_3, Fe_2O_3 and NiO NP surfaces. Less adsorption is observed with TiO_2, which has the lowest PZC in the series (below that of physiological pH = 7.4), appearing at the leading edge of the BE envelope, indicative of adsorbed hydroxyls at ~532 eV.

Table 2. The Available Particle Surface Binding Sites as Quantified by Integrated XPS Peak Area Ratios of Adsorbed-to-Metal Oxide Oxygen Intensity from the O 1s Orbital at pH = 7.4. Reproduced with permission from reference (*28*). Copyright 2013 Elsevier.

metal oxide NP	[adsorbed O]	[metal oxide O]	[adsorbed O/ metal oxide O]
TiO_2	5354.5	9637.6	0.56
Cr_2O_3	12710.5	4101.5	3.10
Mn_2O_3	4381.9	6144.2	0.71
Fe_2O_3	4935.2	4671.6	1.06
NiO	6977.3	2997.0	2.33
CuO	7419.6	1117.8	6.64
ZnO	10551.1	1560.0	6.76

Discussion

We apply insights gained in our study (*vide supra*) to two case studies correlating the role of surface charge and structure with cytotoxicity.

Case I: TiO₂ NPs Induce Dysfunction and Activation of Phagocytic Human Endothelial Cells

Recent studies indicate that NPs with a positive surface charge have a much higher cell internalization ability than NPs with negatively charged surfaces among non-phagocytic cells. Meanwhile, phagocytic cells preferentially uptake NPs with negatively charged surfaces more readily than for positively charged NPs (*44*). This trend for non-phagocytic cells is consistent with findings in this current study for the BEAS-2B and A549 cell lines (*vide supra*). Furthermore, since TiO₂ NPs would adopt a negative surface charge at pH = 7.4, they would likely be more amenable to be incorporated into phagocytic cells as predicted by our observed trends (Figure 3).
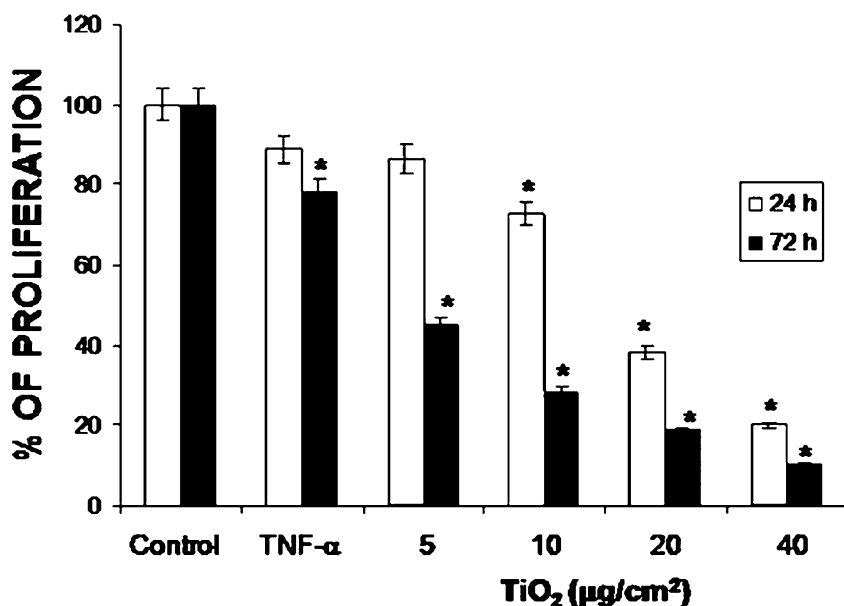

Figure 5. TiO₂ inhibited cell proliferation after 24 and 72 hrs. Reproduced with permission from reference (45). Copyright 2012 American Chemical Society.
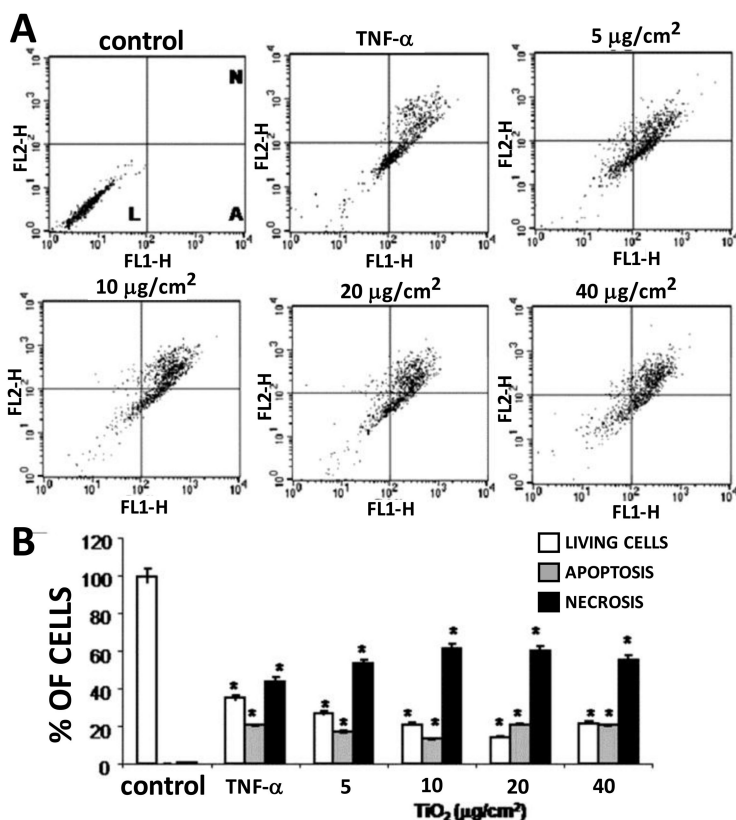
*Figure 6. TiO² induced apoptosis and necrosis. The results are shown as dot
blots (A) or percentage of HUVEC in each quadrant (B). Reproduced with
permission from reference (45). Copyright 2012 American Chemical Society.*

This prediction is confirmed in a study by Montiel-Dávalos et al. (*45*), in
which TiO$_2$ NPs induced dysfunction and activation of human endothelial cells.
In the assay performed, the NPs (< 50 nm in size, and a −6.98 mV zeta potential)
were exposed to human umbilical vein endothelial cells (HUVECs) (*46*). Cell
viability is determined by measuring HUVEC proliferation as evaluated by crystal
violet staining. Decrease in cell proliferation signifies greater toxicity. HUVEC
were plated on 96-multiwell plates and cultured with and without TiO$_2$ NPs for
24 and 72 hrs. The results are plotted in Figure 5, expressed as mean ± SD of
three separate measurements. The asterisks denote a P value < 0.01 as compared
to the control cells. [The P value is a statistical parameter signifying the validity
of the result. Since it is small (< 0.01), there is strong evidence against the null
hypothesis, i.e., there is significant difference between the specified populations.]

The TiO$_2$ NPs inhibit cell proliferation both in a concentration- and time-dependent manner. A maximal effect is seen with an inhibition of 90% at a 40 µg/cm^2 density for 72 hrs. TiO$_2$ has a stronger effect as compared with tumor necrosis factor α (TNF-α) (10 ng/mL concentration), which was used as a positive control for endothelial activation. We postulate that the negative surface charge, as indicated by the measured –6.98 mV zeta potential of the TiO$_2$ NPs, is the driving force for Coulombic attraction of the HUVECs to the NPs, resulting in the decreased cell proliferation due to the resulting cytotoxicity.
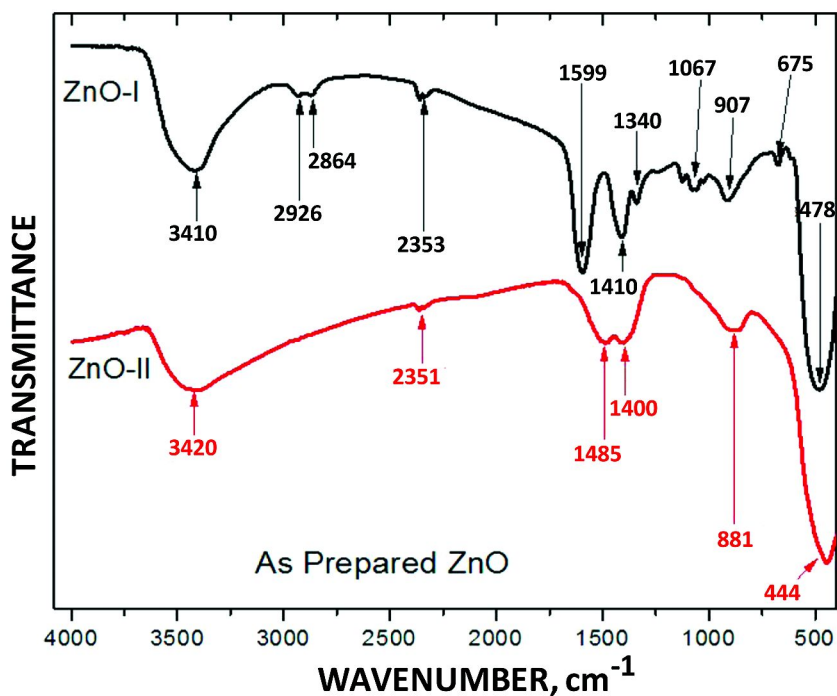

Figure 7. FTIR spectra of ZnO-I and ZnO-II NP. Reproduced with permission from reference (46). Copyright 2014 American Chemical Society.

Cell death of these HUVECs were determined using phosphatidylserine translocation to quantify apoptosis. Cells have been treated with TiO$_2$ NPs for 24 hrs prior to analysis via flow cytometry, and analyzed using a 488 nm (excitation) and 515 nm bandpass filter for fluorescein detection and a filter > 560 nm for propidium iodide detection. Cells stained with annexin-V-fluous alone are considered apoptotic while double-stained cells (annexin-V-fluous +

propidium iodide) are considered as late apoptotic or necrotic cells. The data
(Figure 6) is shown as dot plots (A), or percentage of HUVEC in each quadrant
(B). The letters within each quadrant denote the following: N = necrotic cells,
A = apoptotic cells, L = living cells. Results correspond to a representative
experiment of 3 independent assays. The asterisks denote a P value < 0.01 as
compared to control cells (TNF-α). After a 24-hr exposure the TiO_2 NPs induces
apoptic cell death in ~20% of the HUVECs and necrotic death in 60% of cells
at all used concentrations, in comparison with the control cells. The increase in
necrosis is more pronounced than that of TNF-α-induced necrosis. We attribute
the negative surface charge of the TiO_2 NPs to be the major governing factor
inducing the observed cell death.

Case II: ZnO NPs Can Be Reduced by Lowering the PZC and Relative Number of Surface Binding Sites

ZnO NPs are used extensively in many nanotechnology applications, yet is
among the most toxic of the fourth period transition metal oxides. Because of the
raised environmental health concern, there is an impetus to produce safer ZnO NPs
while preserving their unique optical, electronic and structural properties. One
approach to achieve this end is to tune the NP surface charge and alter its structural
binding sites that interact with the cellular matrix.

A recent report by Punnoose et al. (*46*) has done precisely this, in accord
with predictive trends observed in our study (*vide supra*). Two types of ZnO
NPs were synthesized with different surface properties in terms of charge and
relative number of surface binding sites in aqueous solution media. In comparing
the two differently synthesized ZnO NPs, the one with the higher zeta potential
(i.e., more positive surface charge, and relatively larger number of binding sites)
results in a 1.5-fold increase in cytotoxicicity, in agreement with our predictive
model for non-phagocytic cells. Two equally-sized (9.26 ± 0.11 nm) ZnO NP
samples were synthesized from zinc acetate using a forced hydrolysis process
with their surface chemical structures modified using different reaction solvents.
The resulting structures, analyzed using FTIR spectroscopy, reveal the surface
compositional structures of ZnO-I and ZnO-II NPs (Figure 7). The spectra show
differing degrees of surface hydroxylation between the two NPs. Characteristic
Zn-O vibrations at 478 cm^{-1} for ZnO-I and 444 cm^{-1} for ZnO-II (*47*). The Zn:O
ratio of the NPs are influenced by surface bound chemical groups resulting in
a 34 cm^{-1} difference in vibrational frequency. Broad adsorption at 3410—3420
cm^{-1} is due to attachment of hydroxyl groups to the NP surface, which are more
pronounced in ZnO-I than for ZnO-II. Coordination of atoms on the surface of
ZnO NPs differ from that of their bulk structure. Absorption at 2351—2353 cm^{-1}
is due to absorbed CO_2. ZnO-I exhibits two strong bands, associated with the
carboxylate functional group at 1412 and 1595 cm^{-1}, denoting symmetric and
assymetric stretches, respectively (*48–50*). ZnO-II NPs show these same bands
from surface adsorbed groups from the acetate precursors, but with somewhat
lower intensity and slightly different frequency. In comparing the degree of
absorption on the NP surfaces as a measure of the relative number of binding
sites [in the same manner as in our study using XPS (Figure 4)], the ZnO-I NP

surface has a relatively higher relative number of surface binding sites than that of ZnO-II with which to interact with cells. Hence, a relatively higher cytotoxicity would be predicted for cells coming into contact with ZnO-I than for ZnO-II NPs. This prediction is confirmed by the cytotoxicity assays comparing the two ZnO NPs (*vide infra*). The higher isoelectric point of ZnO-I as compared to ZnO-II also contributes to its higher cytotoxicity. Figure 8 shows zeta potential plots of the two NPs as a function of pH. The zeta potential of the ZnO-I NPs is significantly higher than those values for ZnO-II NPs, at +42.6 mV and +12.5 mV, respectively, under pH = 7.5, which is near the physiological pH. Due to the higher isoelectric point, ZnO-I NPs would adopt a stronger net positive charge at physiological pH as compared to ZnO-II NPs. Therefore, ZnO-I would have a greater Coulombic attraction to cellular material, and hence exhibit greater cytotoxicity among non-phagocytic cells. This trend is also consistent with our PZC results indicating that NPs with higher PZC (i.e., isoelectric point) have a corresponding increase in cytotoxicity (Figure 3).
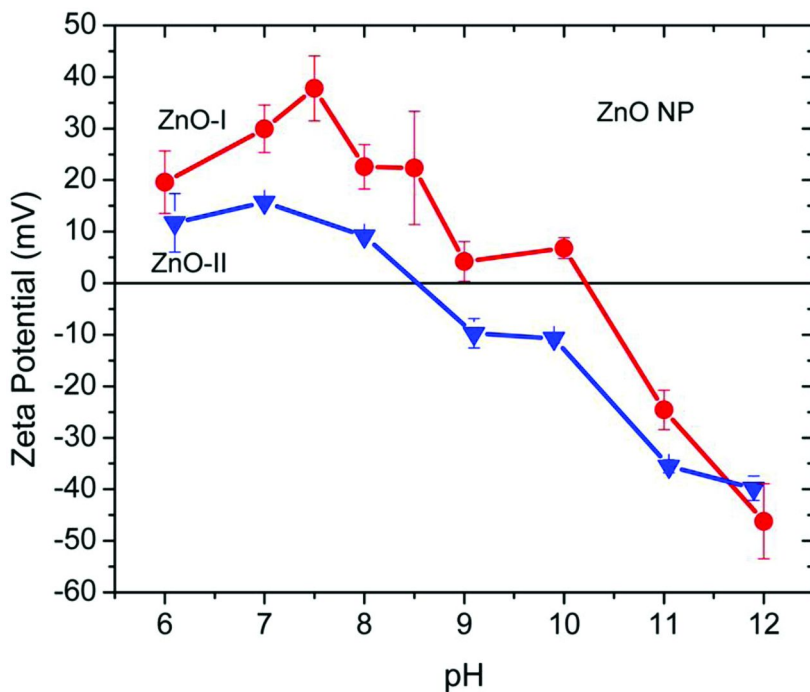

Figure 8. Zeta potentials of ZnO-I and ZnO-II NP measured as a function of pH. Reproduced with permission from reference (46). Copyright 2014 American Chemical Society.
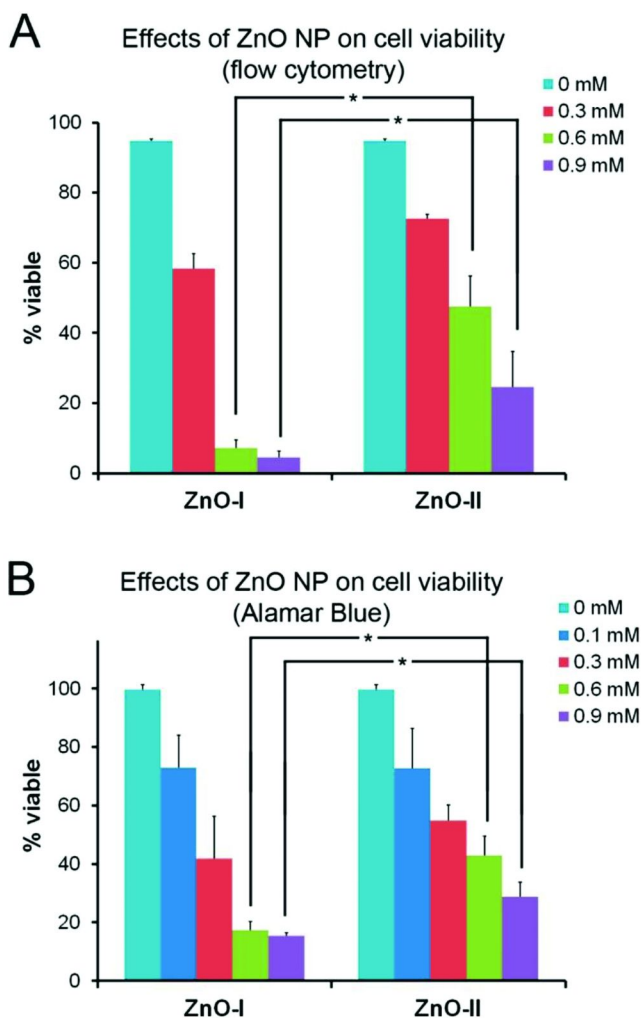
*Figure 9. (A) and (B) display the cell viability of Hut-78 cancer cells after treating with ZnO-I and ZnO-II nanoparticles for 24 hrs at the concentrations indicated, determined using PI-flow cytometry and Alamar Blue methods, respectively. Error bars represent the mean ± standard error of three replicate experiments. Viability between the 2 types are significantly different (*P < 0.05). Reproduced with permission from reference (46). Copyright 2014 American Chemical Society. (see color insert)*

To examine differences between the two ZnO NP cytotoxicities, Hut-78 lymphoma T cells were used for the assays. The non-phagocytic Hut-78 cancer cells were treated with each of the ZnO NPs using two different assays: a propidium iodide (PI) assay and an Alamar blue assay. In the PI-flow cytometry, ZnO NP concentrations of 0, 0.3, 0.6 and 0.9 mM were used with cell viability determined after a 24-hr exposure (Figure 9A). A rapid decrease in cell viability

is observed for increasing concentrations of both ZnO-I and ZnO-II. The ZnO-I NPs exhibits a more rapid reduction in cell viability than ZnO-II NPs. The IC_{50} of ZnO-I and ZnO-II are 0.37 mM and 0.56 mM, respectively. In addition, independent experiments using an Alamar Blue assay applying 0, 0.1, 0.3, 0.6 and 0.9 mM ZnO concentrations yield the same trend, but with slightly lowered IC_{50} values with 0.31 mM for ZnO-I and 0.45 mM for ZnO-II (Figure 9B). In both assays, ZnO-II shows a 1.5 times greater IC_{50} relative to ZnO-I, indicating that ZnO-I NPs are markedly more toxic than ZnO-II NPs. Hence, these cytotoxicity assays confirm the prediction that (i) a greater number of surface binding sites and (ii) higher isoelectric points contribute to greater toxicity of ZnO-I NPs as compared to ZnO-II NPs for non-phagocytic cells.

Conclusions

In summary, the observed toxicity trend in this series of fourth period transition metal oxide NPs (TiO_2, Cr_2O_3, Mn_2O_3, Fe_2O_3, NiO, CuO and ZnO) examined is not cell-type specific within non-phagocytic cells. Instead, cytotoxicity appears to predominantly be a function of NP isoelectric point ($\rho = 0.78$), relative number of available particle surface sites ($\rho = 0.71$) on the NP surface (with Spearman's correlation rank in parentheses). As the A649 and BEAS-2B cell lines show identical trends in toxicity, we predict that the trend will be evident in other non-phagocytic cell lines. Particle surface charge is pH dependent, and may thus influence the rate and routes of their cellular uptake as well as subsequent partitioning between organelles. The relative number of available surface binding sites with cytotoxicity increases the likelihood of NP interaction with biomolecules such as DNA, RNA, protein and lipids. The observed correlation of (i) surface charge and (ii) relative number of binding sites is a useful predictor for relative toxicity as shown by its relevance in the above two discussed case studies. These two variables are important parameters to consider for risk assessment in biological systems.

References

1. McWilliams, A. *NAN031E, BCC Research* **2012**.
2. Noronha, F. B.; Schmal, M.; Nicot, C.; Moraweck, B.; Frety, R. *J. Catal.* **1997**, *168*, 42–50.
3. Chusuei, C. C.; Meier, D. C.; Goodman, D. W. In *Chemical Physics of Solid Surfaces*; Woodruff, D. P., Ed.; Elsevier Science Publishers: London, 2001; Vol. 9, pp 373−408.
4. Chusuei, C. C.; Lai, X.; Luo, K.; Goodman, D. W. *Top. Cat.* **2001**, *14*, 71–83.
5. Roy, S.; Das, D.; Chakravorty, D.; Agrawal, D. C. *J. Appl. Phys.* **1993**, *74*, 4746–4749.
6. Vassiliou, J. K.; Mehrotra, V.; Russell, M. W.; Giannelis, E. P.; Mcmichael, R. D.; Shull, R. D.; Ziolo, R. F. *J. Appl. Phys.* **1993**, *73*, 5109–5116.
7. Prinz, G. A. *J. Magn. Magn. Mater.* **1999**, *200*, 57–68.

8. Airapetyan, S. S.; Balayan, G. G.; Khachatryan, A. G. *Russ. J. Appl. Chem.* **2001**, *74*, 519–521.

9. Kobe, S.; Drazic, G.; McGuiness, P. J.; Strazisar, J. *J. Magn. Magn. Mater.* **2001**, *236*, 71–76.

10. Gruttner, C.; Teller, J. In *Scientific and Clinical Applications of Magnetic Carriers*; Hafeli, U., Schutt, W., Teller, J., Eds.; Plenum Publishing Corporation: New York, 1997, p 53.

11. Osmond, M. J.; McCall, M. J. *Nanotoxicology* **2010**, *4*, 15–41.

12. Rabinow, B.; Chaubal, M. V. *Drugs Pharm. Sci.* **2006**, *159*, 199–229.

13. Korin, N.; Kanapathipillai, M.; Ingber, D. E. *Israel J. Chem.* **2013**, *53*, 610–615.

14. Oberdorster, G.; Oberdorster, E.; Oberdorster, J. *Environ. Health Perspect.* **2005**, *113*, 823–839.

15. Huang, C. C.; Aronstam, R. S.; Chen, D. R.; Huang, Y.-W. *Toxicol. In Vitro* **2010**, *24*, 45–55.

16. Wang, H. J.; Growcock, A. C.; Tang, T. H.; O'Hara, J.; Huang, Y.-W.; Aronstam, R. S. *Toxicol. In Vitro* **2010**, *24*, 1953–1961.

17. Nooney, M. G.; Murrell, T. S.; Corneille, J. S.; Rusert, E. I.; Hossner, L. R.; Goodman, D. W. *J. Vac. Sci. Technol., A* **1996**, *14*, 1357–1361.

18. Nooney, M. G.; Campbell, A.; Murrell, T. S.; Lin, X.-F.; Hossner, L. R.; Chusuei, C. C.; Goodman, D. W. *Langmuir* **1998**, *15*, 2750–2755.

19. Chusuei, C. C.; Goodman, D. W.; Van Stipdonk, M. J.; Justes, D. R.; Loh, K. H.; Schweikert, E. A. *Langmuir* **1999**, *15*, 7355–7360.

20. Brunauer, S.; Emmett, P. H.; Teller, E. *J. Am. Chem. Soc.* **1938**, *60*, 309–319.

21. Brown, G. E., Jr.; Henrich, V. E.; Casey, W. H.; Clark, D. L.; Eggleston, C.; Felmy, A.; Goodman, D. W.; Grätzel, M.; Maciel, G.; McCarthy, M. I.; Nealson, K. H.; Sverjensky, D. A.; Toney, M. F.; Zachara, J. M. *Chem. Rev.* **1999**, *99*, 77–174.

22. Park, J.; Regalbuto, J. R. *J. Colloid Interface Sci.* **1995**, *175*, 239–252.

23. McPhail, M. R.; Sells, J. A.; He, Z.; Chusuei, C. C. *J. Phys. Chem. C* **2009**, *113*, 14102–14109.

24. Barr, T. L. *Modern ESCA*; CRC Press: Boca Raton, 1994.

25. Barr, T. L.; Seal, S. *J. Vac. Sci. Technol., A* **1995**, *13*, 1239–1246.

26. Shirley, D. A. *Phys. Rev. B* **1972**, *5*, 4709–4714.

27. Lin, W.; Xu, Y.; Huang, C. C.; Ma, Y.; Shannon, K. B.; Chen, D. R.; Huang, Y.-W. *J. Nanopart. Res.* **2009**, *25*, 451–457.

28. Chusuei, C. C.; Wu, C.-H.; Mallavarapu, S.; Stephen Hou, F. Y.; Hsu, C.-M.; Winiarz, J. G.; Aronstam, R. S.; Huang, Y.-W. *Chem.-Biol. Interact.* **2013**, *206*, 319–326.

29. Oku, M.; Hirokawa, K. *J. Electron Spectrosc. Relat. Phenom.* **1975**, *7*, 465–473.

30. Strohmeier, B. R.; Hercules, D. M. *J. Phys. Chem.* **1984**, *88*, 4922–4929.

31. Haber, J.; Stoch, J.; Ungier, L. *J. Electron Spectrosc. Relat. Phenom.* **1976**, *9*, 459–467.

32. McIntyre, N. S.; Zetaruk, D. G. *Anal. Chem.* **1977**, *49*, 1521–1529.

33. Wagner, C. D.; Zatko, D. A.; Raymond, R. H. *Anal. Chem.* **1980**, *52*, 1445–1451.

34. Slinkard, W. E.; DeGroot, P. B. *J. Catal.* **1981**, *68*, 423–432.
35. Gonbeau, D.; Guuimon, C.; Pfister-Guillouzo, G.; Levasseur, A.; Meunier, G.; Dormoy, R. *Surface Sci.* **1991**, *254*, 81–89.
36. Wagner, C. D.; Riggs, W. M.; Davis, L. E.; Moulder, J. F.; Muilenbuerg, G. E. *Handbook of X-ray Photoelectron Spectro-scopy*; Perkin-Elmer Corporation: Eden Prairie, MN, 1979.
37. Khawaja, E. E.; Salim, M. A.; Khan, M. A.; Al-del, F. F.; Khatak, G. D.; Hussain, Z. XPS, Auger, electrical and optical studies of vanadium phosphate glasses doped with nickel oxide. *J. Non-Cryst. Solids* **1989**, *110*, 33–43.
38. Howng, W.-Y.; Thorn, R. J. *J. Phys. Chem. Solids* **1980**, *41*, 75–81.
39. Ertl, G.; Hierl, R.; Knozinger, H.; Thiele, N.; Urbach, H. P. *Appl. Surf. Sci.* **1980**, *5*, 49–64.
40. Otamiri, J. C.; Andersson, S. L. T.; Andersson, A. *Appl. Catal.* **1990**, *65*, 266–279.
41. Strohmeier, B. R.; Hercules, D. M. *J. Catal.* **1984**, *86*, 266–279.
42. Henrich, V. E.; Cox, P. A. *The Surface Science of Metal Oxides*; Cambridge University Press: New York, 1994.
43. Perry, D. L.; Tsao, L.; Taylor, J. A. *Inorg. Chim. Acta* **1984**, *85*, L57–L60.
44. Fröhlich, E. *Int. J. Nanomed.* **2012**, *7*, 5577–5591.
45. Montiel-Dávalos, A.; Ventura-Gallegos, J. L.; Alfaro-Moreno, E.; Soria-Castro, E.; Garcia-Latorre, E.; Cabañas-Moreno, J. G.; del Pilar Ramos-Godinez, M.; López-Marure, R. *Chem. Res. Toxicol.* **2012**, *25*, 920–930.
46. Punnoose, A.; Dodge, K.; Rasmussen, J. W.; Chess, J.; Wingett, D.; Anders, C. *ACS Sustain. Chem. Eng.* **2014**, *2*, 166–1673.
47. Farbun, I. A.; Romanova, I. V.; Terikovskaya, T. E.; Dzanashvili, D. I.; Kirillov, S. A. *Russ. J. Appl. Chem.* **2007**, *80*, 1798–1803.
48. Bian, S.-W.; Mudunkotuwa, I. A.; Rupasinghe, T.; Grassian, V. H. *Langmuir* **2011**, *27*, 6059–6068.
49. Max, J. J.; Chapados, C. *J. Phys. Chem. A* **2002**, *106*, 6452–6461.
50. Max, J. J.; Chapados, C. *J. Phys. Chem. A* **2004**, *108*, 3324–3337.